# Charge Transfer, Luminescence, and Phonon Bottleneck in TiO$_2$ Nanowires Computed by Eigenvectors of Liouville Superoperator

Shuping Huang and Dmitri S. Kilin*

Department of Chemistry, University of South Dakota, Vermillion, South Dakota 57069, United States

S *Supporting Information*

ABSTRACT: A nonadiabatic excited state dynamics study of ⟨001⟩ anatase TiO$_2$ nanowire is obtained by combining density matrix in Liouville−Redfield formalism and ab initio electronic structure calculations. The properties of eigenvectors of Liouville−Redfield superoperator are investigated. The time evolutions of Kohn−Sham orbital populations are obtained for different electronic excitations. The numerical solutions of the population changes over time are in agreement with the analytical results. The analytical and numerical results on the electron and hole relaxation rates are compared. The electron nonradiative relaxation to the bottom of conduction band involves Ti 3d orbitals, whereas the hole nonradiative relaxation to the top of valence band is mainly localized in surface O 2p orbitals. The rate of relaxation in nanowire is slower than in bulk TiO$_2$ demonstrating phonon-bottleneck effect. Calculated emission spectrum has vanishing contribution from lowest energy excitation, which indicates charge transfer.
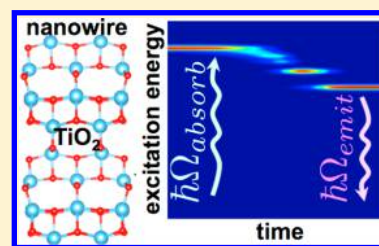
1. INTRODUCTION

Oxide semiconductors, including titanium dioxide (TiO$_2$), are being considered as a replacements for silicon in the development of the next generation of solar cells.[1] TiO$_2$ has received considerable attention due to its wide application in both energy and environmental fields, such as photo-catalysis,[2−4] self-cleaning material, and electrode in dye-sensitized solar cells (DSSCs).[5,6] A desirable approach for each of these applications includes harvesting energy directly from sunlight and efficiently separating electron and hole. In photocatalysis: first, the semiconductor material absorbs sunlight and generates an electron−hole pair; then the electron and hole are transferred to surface reaction sites, which are usually separated spatially, to complete a reduction/oxidation reaction.

The ability of TiO$_2$ nanoparticles to produce oxygen by photocatalytic water oxidation was first reported by Fujishima and Honda.[2] TiO$_2$ has three major structure forms: anatase, rutile, and brookite. Among them, anatase has generally shown higher photocatalytic activity than rutile and has a bandgap of about 3.2 eV.[7] Rutile phase is the most stable for bulk, whereas anatase appears to be more stable than rutile for TiO$_2$ nanoparticles.[8,9] Nanosized structures offer unique character-istics that are greatly influenced by their diameters,[10] crystallographic orientations,[11] surface passivation,[12] presence of dopants,[4,13,14] and so forth.

Although theoretical studies of TiO$_2$ bulk and surfaces have been extensively carried out,[15−25] there is relatively little study on anatase TiO$_2$ nanowires (NWs). Lewis et al. investigated the structural and electronic properties of thin anatase NWs with ⟨001⟩ growth direction by ab initio density functional theory method.[26] They showed that the perimeter of NWs is an important dimensional parameter in considering stability. Based

on theoretical calculations, Deak et al. have proposed that promising field-effect transistor devices might be realized with thin, Ta-doped anatase ⟨001⟩ NWs.[27] Meng et al.[28] investigated the electronic coupling between a TiO$_2$ NW and a natural dye sensitizer, using real-time time-dependent density functional theory (TDDFT) simulations.

There is much literature on nonadiabatic coupling calculations due to the fundamental role of radiationless processes in photocatalysis. Computational approaches to nonadiabatic coupling are classified into several types: trajectory-based methods and techniques, direct propagation of the wave function, and approaches based on reduced density operator.[19] The trajectory-based methods include surface-hopping,[29−33] mean-field Ehrenfest,[34] and classical mapping approaches.[35,36] The approaches based on the evolution of the reduced density matrix (RDM) are implemented in the form of multilevel Redfield theory[37−41] and the noninteracting blip approximation,[42] which serves as a time-dependent general-ization of Förster theory.

Prezhdo et al. investigated the photoinduced electron transfer at molecule-TiO$_2$ interfaces[43−47] using the surface-hopping method.[48−50] Subsequently, the same method has been applied to the more complex interfaces of TiO$_2$ with a water layer,[51] a graphene-layer,[52] and a semiconductor quantum dot.[53] These works have provided an understanding of the mechanisms of electron transfer, relaxation and recombination dynamics, and the effect of these processes on the solar cell efficiencies. Batista et al.[54] explored the process of electron injection in catechol/TiO$_2$-anatase nanostructures at the detailed molecular level to gain a fundamental understanding

of excited-state electron-injection paths by propagating wave function in time. Inerbaev et al.[19] have presented theoretical and computational treatment of charge transfer at the Ru-doped wet anatase (100) TiO_2 surface based on reduced density matrix and Redfield theory.

Each of types of methods takes into account an average over ensemble of configurations of ions. Trajectory-based methods perform such average explicitly by adding together dynamics for various trajectories. Direct propagation methods perform such average implicitly, at the stage of deriving equation of motion for density matrix and treating ionic degrees of freedom as bath specifically. Upon averaging over the ensemble of possible configurations of ions, the terms linear in nonadiabatic coupling vanish due to sign alternation. The lowest nonvanishing contribution is by a second order of electron-to-lattice coupling.[55] Dynamics of most important observables is determined by a second power of a coupling, similar to the Fermi golden rule. The Redfield tensor summarizes all possible second order processes in respect to electron–nuclear coupling and seems to be helpful for intuitive interpretation and comparison of elementary electronic transitions.

Open challenges in design of efficient materials for photovoltaic and photoelectrochemical cells prompt a need to control lifetime of charge transfer excitations. This challenge is most efficiently addressed by Redfield dynamics method to nanosystems.

Electron–phonon coupling controls nonradiative relaxation dynamics of the photoexcited electron–hole pair in semiconductor nanostructures. In this work, we theoretically investigate the nonadiabatic excited state dynamics of bare anatase TiO_2 NW by the reduced density operator formalism to elucidate electron-transfer pathways together with energy losses due to lattice induced charge carrier relaxation. This research is motivated by a need to see how quantum confinement affects nonradiative lifetime of charge-transfer states in bare NWs. In our other works on relaxation in TiO_2 nanostructures, we observe drastic qualitative changes in the energy gap law.[56−58] We attempt to provide an insight on relaxation rate dependence on excitation energy for models with different confinement regimes. The present report on bare TiO_2 NW is intended to give a reference point to the research program on surface modified NWs.

2. COMPUTATIONAL METHOD

A. Density Functional Theory (DFT) Calculations. The DFT calculations are based on the fictitious one-electron Kohn−Sham (KS) equation[59]

$$\left\{-\frac{\nabla^2}{2} + v_{KS}[\rho](r)\right\}\varphi_i(r) = \varepsilon_i\varphi_i(r) \tag{1a}$$

$$\rho(r) = \sum_i^{OCC} |\varphi_{i(r)}|^2 \tag{1b}$$

$$v_{KS}[\rho](r) = v_{ext}(r) + v_{Hartree}[\rho](r) + v_{xc}[\rho](r) \tag{1c}$$

An initial guess density $\rho_0(r)$ is first supplied to evaluate the KS potential $v_{KS}[\rho](r)$. Each component of KS potential is calculated separately and each poses a different numerical problem. The exchange-correlation potential is defined as $v_{xc}[\rho](r) = \delta E_{xc}/\delta\rho(r)$. There are many approximate exchange-correlation functionals, such as local-density approximation (LDA),[60] generalized gradient approximation (GGA),[61,62] and

hybrid functionals which mix exact (i.e., Hartree−Fock) and DFT exchange and describe correlation at the DFT level.[63]

When KS potential is calculated, one can solve eq 1a to obtain the eigenstates $\varphi_i(r)$ of Hamitonian H_{KS}. The new density form is obtained via eq 1b. The self-consistency cycle is stopped when the convergence criterion is reached. If the criteria have not been fulfilled, a self-consistency cycle with a new density is restarted.

The DFT calculations are performed by the Vienna ab initio simulation package (VASP).[64] We adopted the Perdew−Burke−Ernzerhof (PBE) form[62] of GGA with the projected augmented wave (PAW) potentials.[65] We placed the TiO_2 NW in a supercell and separated it from its image in the neighboring supercell by a vacuum region of 9 Å. Artificial periodic boundary conditions are imposed in the ⟨100⟩ and ⟨010⟩ directions for ⟨001⟩ NW. There are 25 Ti atoms and 50 O atoms in each unit cell. A full relaxation of the ionic positions with no symmetry constraints on the NW structure was performed by conjugate-gradient algorithm. Cutoff energies of 430 eV were used. Only Γ (0.0, 0.0, 0.0) point was sampled in Brillouin zone.

The transition dipole moments, oscillator strength, and absorption spectra are calculated from KS orbitals as mentioned in our previous work.[66,67]

The optimized structure was heated to 300 K for 150 fs before adiabatic MD calculations. To keep the needed kinetic energy of the model constant, the velocities of all the atoms are rescaled to simulate a constant temperature during the heating process according to $\sum_{I=1}^{N} M_I((d\mathbf{R}_I/dt)|_{t=0})^2/2 = 3/2Nk_BT$, where M_I and $d\mathbf{R}_I/dt$ stand for the mass and initial velocity of Ith nucleus, respectively, N is a number of nuclei, k_B is the Boltzmann constant, and T is the temperature. In the MD simulation, the time step was set to 1.0 fs. The atomic trajectories from a 1 ps adiabatic MD simulation in the microcanonical ensemble are used to perform nonadiabatic coupling calculations.

B. Reduced Density Matrix and Redfield Equation. For a total system that consists of a subsystem of interest and a bath, the total Hamiltonian $\hat{H}$ can be written as a sum of the subsystem part $\hat{H}_s$, the bath part $\hat{H}_b$, and the subsystem−bath interaction $\hat{V}$: $\hat{H} = \hat{H}_s + \hat{H}_b + \hat{V}$.[68] The subsystem we studied in this work is electron or hole and the bath are ions. The electron−phonon interaction $\hat{V}$ in the studied system is weak and thus treated in a perturbative way. The density operator for the whole system in its pure state reads: $\hat{\rho}_{tot}(t) = |\Phi(t)\rangle\langle\Phi(t)|$, where $\Phi(t)$ is the state that represents the complete system. Because we are only interested in the subsystem part, the reduced density operator $\hat{\rho}$ for the subsystem is obtained from the density matrix of the complete system through the trace over the bath variables, that is

$$\hat{\rho}(t) = Tr_b\{\hat{\rho}_{tot}(t)\} = \sum_b \langle\varnothing_b(t)|\hat{\rho}_{tot}(t)|\varnothing_b(t)\rangle \tag{2}$$

Here $\varnothing_b(t)$ are the eigenstates of the bath. The equation of motion for the reduced density operator is contributed by Hamiltonian evolution and a term that corresponds to interaction with bath

$$\frac{\partial}{\partial t}\hat{\rho}(t) = \sum_b \left\langle \varnothing_b(t) \left| -\frac{i}{\hbar}[(\hat{H}_s + \hat{H}_b + \hat{V}), \hat{\rho}_{tot}(t)] \right| \varnothing_b(t) \right\rangle$$

$$= -\frac{1}{\hbar}[\hat{H}_s, \hat{\rho}(t)] - \frac{i}{\hbar}\sum_b \langle \varnothing_b(t)|[\hat{V}, \hat{\rho}_{tot}(t)]|\varnothing_b(t)\rangle$$

The latter term is represented by second order in V. Then we treat the subsystem density operator and its equation of motion in the basis of KS orbitals φ_i, which gives the density matrix $\rho_{ij} = \langle \varphi_i|\hat{\rho}|\varphi_j\rangle$. The time dependence for the density matrix for a specific initial excitation $\rho_{ij}^{(a,b)}(0)$ where an electron is promoted from the orbital a to the orbital b will be calculated by solving the following equation of motion for electronic degrees of freedom[69−71]

$$\dot{\rho}_{ij} = [(\hat{\mathcal{L}} + \hat{\mathcal{R}})\hat{\rho}]_{ij} \tag{3a}$$

$$(\hat{\mathcal{L}}\hat{\rho})_{ij} = -\frac{i}{\hbar}\sum_k (F_{ik}\rho_{kj} - \rho_{ik}F_{kj}) \tag{3b}$$

$$(\hat{\mathcal{R}}\hat{\rho})_{ij} = \left(\frac{d\rho_{ij}}{dt}\right)_{diss} = \sum_{kl} R_{ijkl}\rho_{kl} \tag{3c}$$

$\hat{\mathcal{L}}$ and $\hat{\mathcal{R}}$ are Liouville and Redfield superoperators, respectively. Equation 3b includes the one-electron energy operator $\hat{F} = \hat{F}^{(KS)} - \vec{D}\cdot\vec{\varepsilon}(t)$, with $\vec{D}$ as the electric dipole vector of the system and $\vec{\varepsilon} = \vec{\varepsilon}_0\cos\Omega t$ as an electric field of incident light. The effective Hamiltonian $\hat{F}$ describes electrons but does not include an electron−phonon coupling. The second term refers to electronic dissipative transitions, which are facilitated by thermal fluctuation of ions. Diagonal elements of the density matrix correspond to state population and off-diagonal elements of density matrix give quantum coherences. In this work, only diagonal elements of the density matrix are considered. The influence of the nuclear motion on electronic degrees of freedom is contained entirely in the Redfield relaxation tensor, $\hat{\mathcal{R}}$. The physical interpretation of the Redfield tensor element R_{ijkl} is essentially a rate constant that relates the rate of change of density matrix element ρ_{ij} to the current value of each other density matrix element ρ_{kl}.[40] The R_{iijj} represents the rate of population transfer from state |j> to state |i>, and it is abbreviated to R_{ij} in this work. The charge density distribution can further be obtained from eq 3a−3c, as well as the rate of energy dissipation and the rate of charge transfer.

The Redfield tensor is defined in terms of electron−nuclear coupling. On-the-fly nonadiabatic couplings are computed along nuclear trajectory as[72]

$$V_{ij}(t) = -i\hbar\left\langle \varphi_i^{KS} \left| \frac{d}{dt} \right| \varphi_j^{KS} \right\rangle$$

$$= \frac{-i\hbar}{2\Delta t}\int d\vec{r}[\varphi_i^{KS*}(\{\vec{R}_I(t)\}, \vec{r})\varphi_j^{KS}(\{\vec{R}_I(t+\Delta t)\}, \vec{r})$$

$$- \varphi_i^{KS*}(\{\vec{R}_I(t+\Delta t)\}, \vec{r})\varphi_j^{KS}(\{\vec{R}_I(t)\}, \vec{r})] \tag{4}$$

The nonadiabatic couplings are then processed with an autocorrelation function

$$M_{ijkl}(\tau) = \frac{1}{T}\int_0^T dt V_{ij}(t+\tau)V_{kl}(t) \tag{5a}$$

A Fourier transform of coupling autocorrelation function provides components $\Gamma^{\pm}$

$$\Gamma_{ijkl}^+ = \int d\tau M_{ijkl}(\tau)\exp(-i\omega_{kl}\tau) \tag{5b}$$

$$\Gamma_{ijkl}^- = \int d\tau M_{ijkl}(\tau)\exp(-i\omega_{ij}\tau) \tag{5c}$$

These components add together and compose Redfield tensor, which controls dynamics of density matrix

$$R_{ijkl} = \Gamma_{ljik}^+ + \Gamma_{ljik}^- - \delta_{lj}\sum_m \Gamma_{immk}^+ - \delta_{ik}\sum_m \Gamma_{lmmj}^- \tag{5d}$$

We assume that for nonequilibrium initial conditions, time evolution of density matrices takes form: $\rho^v(t) = \rho^v e^{\Omega_v t}$, which was substituted into eq 3a. Then we obtain the following equation:

$$(\hat{\mathcal{L}} + \hat{\mathcal{R}})\rho^v = \Omega_v\rho^v \tag{6a}$$

ν is a set of parameters labeling the eigen-states for electron or hole. The diagonalization of Liouville−Redfield superoperator is performed. The superposition of eigenvectors ρ^v are used to compose the density matrix for each instant of time

$$\hat{\rho}(t) = \sum_v c_v\rho^v e^{\Omega_v t} \tag{6b}$$

In specific basis of KS orbitals $\rho_{ij} = \langle \varphi_i|\hat{\rho}|\varphi_j\rangle$, eq 6b reads

$$\rho_{ij}(t) = \sum_v c_v\rho_{ij}^v e^{\Omega_v t} \tag{6c}$$

At each time, $\sum_v\rho_{ii}^v(t) = 1$. The expansion coefficient c_v is the proportion of the eigenstate ρ^v contributing to the solution for given initial condition: $\sum_v\rho_{ii}^v c_v = \rho_{ii}^{(a,b)}(t=0)$.

C. Dynamics of the Intraband Nonadiabatic Relaxation. A nonequilibrium charge density distribution in the energy and time domain reads $n^{(a,b)}(\varepsilon,t) = \sum_i\rho_{ii}^{(a,b)}(t)\delta(\varepsilon_j - \varepsilon)$, where (a,b) denotes the initial photoexcitation from state a to state b. The relative change of population with respect to the equilibrium distribution is as follows:

$$\Delta n^{(a,b)}(\varepsilon, t) = n^{(a,b)}(\varepsilon, t) - n^{eq}(\varepsilon, t) \tag{7}$$

This equation describes a population gain when $\Delta n > 0$ and a loss when $\Delta n < 0$ at energy ε.

The e and h refer to the electron in the conduction band and the hole in the valence band, respectively. Below, we use index e with an understanding that the equations for holes are the same for electrons.

Expectation value of energy of a carrier (electron or hole)

$$\langle\Delta\varepsilon_e\rangle(t) = \sum_{i\in CB}\rho_{ii}(t)\varepsilon_i(t) \tag{8}$$

The above formula can be rewritten in terms of dimensionless energy

$$\langle E_e\rangle(t) = \frac{\langle\Delta\varepsilon_e\rangle(t) - \langle\Delta\varepsilon_e\rangle(\infty)}{\langle\Delta\varepsilon_e\rangle(0) - \langle\Delta\varepsilon_e\rangle(\infty)} \tag{9}$$

Assuming single exponential fit of the energy dissipation

$$\langle E_e\rangle(t) = \exp\{-k_e t\} \tag{10}$$

Energy dissipation rate can be expressed as follows

$$k_e = \{\tau^e\}^{-1} = \left\{ \int_0^\infty \langle E_e \rangle(t) dt \right\}^{-1} \qquad (11)$$

This work applies the following approximations: the ions are considered as point charges, the lattice vibrations abruptly equilibrate with a thermostat, the coupling autocorrelation function decays instantaneously, as shown in what follows, leading to the Markov approximation, the vibrational reorganization is neglected, and the excited and ground state potential energy surfaces are assumed to have the same profiles (classical path approximation). One needs additional tests to justify validity of used approximations. Uniqueness is that eigenvalue analysis is an efficient substitution of numerical integration of the equation of motion.

DFT is numerically inexpensive. Validity of KS basis for nonadiabatic couplings is discussed in literature by Fisher et al.[73] From the practical viewpoint, the KS orbital basis proved to be very useful to nonadiabatic excited state dynamics simulations for many systems (molecules, semiconductors, nanotubes, etc.).[54] According to Burke,[74] KS orbitals serve as an adequate basis for computing transport at molecular junctions. It is important to note that KS orbitals are not used as electronic states. KS orbitals are used as a basis. In this work, we solve Redfield equation by diagonalizing Liouville−Redfield superoperator, in an analogy to solving for roots of Casida Equation in TDDFT. Diagonalization of the superoperator provides dissipative eigenstates of the system. Those eigenstates are composed of KS orbitals and the actual, physical states are obtained as superposition of the eigenstates of Liouville−Redfield superoperator, which match the initial condition.

3. RESULTS AND DISCUSSION

Figure 1, panels a−c show the top view and side view of the minimum energy geometry of NW at 0 K and the top view of the geometry at 1000 fs in MD calculation. After the geometry relaxation, the largest changes occur in the outer region (Figure
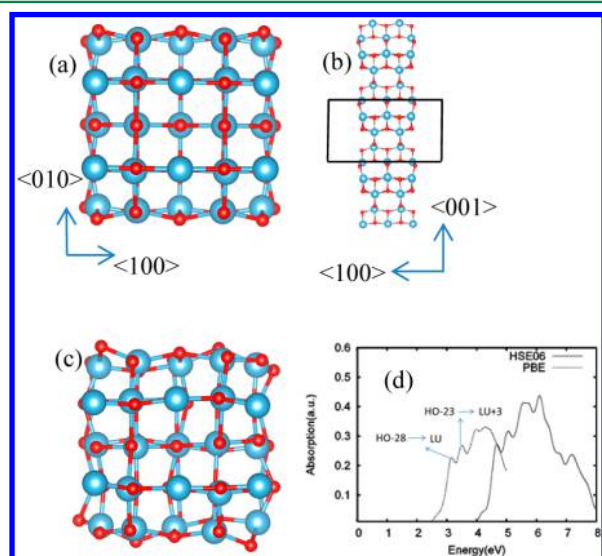

Figure 1. (a) Top view and (b) side view of the simulation NW optimized at 0 K. The box represents each unit cell used in our calculations. (c) Top view of the NW at 1000 fs in MD. The direction is the same as shown in panel (a). Ti atoms are in blue, and O atoms are in red. (d) Calculated absorption spectra of the bare NW by PBE (dashes) and HSE06 (solid line) functionals.

1a). The surface atoms in the bare nanowire relax substantially: all Ti atoms move inward and most O atoms move outward. Molecular dynamics at ambient temperature affect the system geometry (Figure 1c). The average distance of Ti−O bonds become larger in the MD simulations and the atoms in the inner region are also distorted.

The calculated band gaps of anatase TiO_2 bulk and bare ⟨001⟩ NW by GGA-PBE functional are 1.91 and 2.20 eV, respectively. The calculated energy gaps are underestimated due to the self-interaction problem, the discontinuity of the exchange correlation potential,[75] and incorrect description of the asymptotic behavior by GGA exchange-correlation potentials.[76] The Heyd−Scuseria−Ernzerhof (HSE) screened Coulomb hybrid density functional,[63] which contains 25% exact exchange at short-range, offers a better description of band gaps. The calculated band gaps of TiO_2 bulk and bare ⟨001⟩ NW by the HSE06 functional are 3.49 and 3.67 eV, respectively. As shown in Figure 1d, the calculated absorption edge of ⟨001⟩ NW by the HSE06 functional is largely blue-shifted compared with the one by the PBE functional. An increase of the gap in NW by 0.18 eV corresponds to quantum confinement. The details of density of states (DOS) and partial DOS for the bare ⟨001⟩ NW is reported in ref 56.

Figure 2 shows the fluctuations of temperature and KS orbital energies during MD simulations. The average temperature in MD simulation is 280.5 K, and the sample standard deviation is 29.8 K. The KS orbital energies oscillate with time at ambient temperature. The energies of highest occupied obital (HO) and lowest unoccupied orbital (LU) fluctuate by 0.62 and 0.40 eV, respectively. Time evolution of KS orbitals provides nonzero probability of transitions between orbitals. Along eqs 4−5, analysis of autocorrelation functions M_{ijkl} of nonadiabatic couplings V_{ij} and Redfield tensor for bare TiO_2 NW is illustrated in Figure 3. Autocorrelations for the (LU + 1, LU + 2), (HO − 1, HO), and (LU, LU + 1) decay abruptly within a few femtoseconds. The autocorrelation for (HO, LU) is close to 0. The maximal absolute values of the representative Redfield tensor element appear at $i = 9$ (LU + 2), $j = 8$ (LU + 1) or $i = 8$, $j = 9$. The transitions in conduction bands are quicker than the ones in valence bands. The element of Redfield tensor connecting states near the bandgap is vanishing.

The eigenstates of the Liouville−Redfield superopertor are important because the time evolution of the density matrix can be decomposed in the basis of the eigenstates (see eq 6b). According to ref 55, in secular limit ρ_{ij} and ρ_{ii} evolve independently. In this approximation, an intraband evolution of electrons, holes, and an interband e-h recombination can be processed independently

$$(\hat{\mathcal{L}} + \hat{\mathcal{R}}) \rightarrow (\hat{\mathcal{L}} + \hat{\mathcal{R}})^{\text{electrons}} + (\hat{\mathcal{L}} + \hat{\mathcal{R}})^{\text{holes}} \\ + (\hat{\mathcal{L}} + \hat{\mathcal{R}})^{\text{interband}} \qquad (12)$$

We apply the formalism to a part of Liouville space, specifically, to diagonal elements of density matrix. Therefore, in what follows we describe ρ_{ij}^ν for $i = j$, that is, ρ_{ii}^ν. Each diagonal element of eigenvector ρ^ν is the proportion of a given orbital contributing to the eigenstate ρ^ν. We observe a specific pattern in eigenvectors of the Liouville−Redfield superoperator. Figure 4 shows several eigenvectors of the Liouville−Redfield superoperator. Each component of the eigenvector takes a value between −1 and 1. The sum of the squares of each element of an eigenvector is equal to 1. For the first eigenvector of both electron and hole, the first element is 1 and all the other
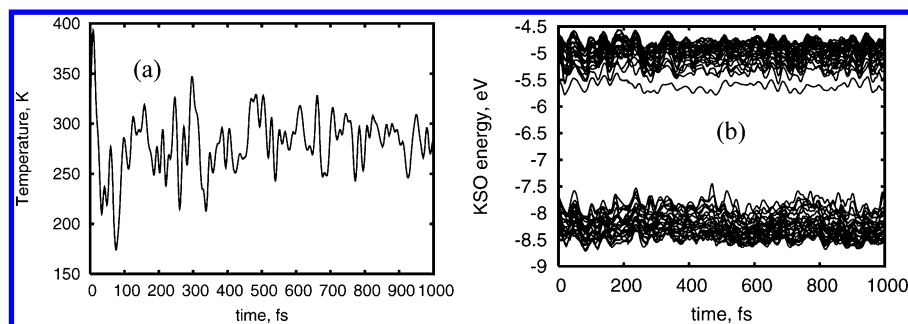
Figure 2. Fluctuations of (a) temperature and (b) KS orbital energies during MD simulations.
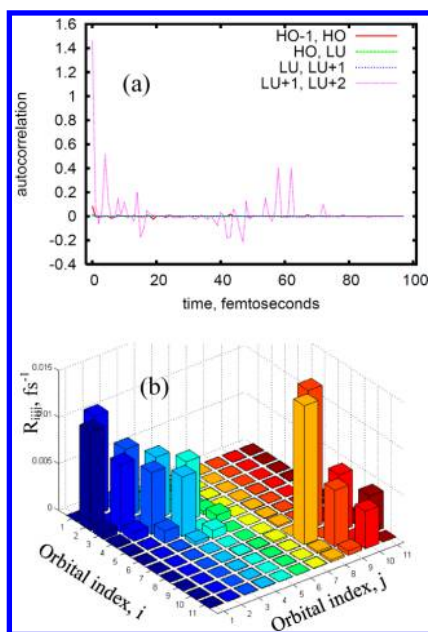

Figure 3. (a) Autocorrelation function of nonadiabatic coupling, for representative transitions $(HO − 1, HO)$, (HO, LU), $(LU, LU + 1)$, and $(LU + 1, LU + 2)$. (b) Representative elements of Redfield tensor, for population transfer in the orbitals near the band gap. $i = j = 6 = HO$, $i = j = 7 = LU$.

elements are 0. For the second eigenvector of both electron and hole, the first element is $−\sqrt{2} = −0.7071$ and the second element is $\sqrt{2} = 0.7071$ with the other elements being 0. The $(n + 1)^{th}$, $(n + 2)^{th}$, ... elements of the nth eigenvector are 0. The values of the nonzero elements of each eigenvector are alternating signs between the plus and the minus, except for the fourth and fifth eigenvectors for electron.

Supporting Information Table S1 lists the eigenfrequencies for different eigenstates of electron and hole. Numerical values of eigenvalues $\Omega = Re\Omega + iIm\Omega$ allow interpretation of the character of dynamics. An imaginary part $Im\Omega \neq 0$ of an eigenvalue corresponds to oscillatory character. Positive real part values of an eigenvalue $Re\Omega > 0$ correspond to thermal excitations. Negative real part values of $Re\Omega < 0$ correspond to relaxation. Zero values of $\Omega = 0$ correspond to absence of dynamics $e^{0·t} = 1 = const$. In the current calculation, for selected part of Liouville space we observe only two cases: relaxation, $Re\Omega < 0$ and quasi-stationary trapping of excitation $\Omega_1^e = \Omega_1^h = 0$.

An analytical solution is practical for a very small number of coupled equations. For a realistic number of considered states one needs to employ a numerical solution. Numerical solution

by time propagation with, for example, Runge−Kutta method does accumulate error and does depend on the number and duration of a time step Δt, giving limits to time interval. Here, we avoid step-by-step propagation by using diagonalization of Liouville operator, which works for time interval of any duration. In order to avoid doubts, we double-checked the agreement of dynamics obtained by analytical solution and by diagonalization of Liouville superoperator.

Case Study: In order to see the reliability of the numerical solution of the time evolution of the orbital populations, we consider the analytical solution of the electron part of a specific excited state $iE = 3$, $iH = 8$ (The electron index iE corresponds to the electron in $LU + iE −1$, and the hole index iH corresponding to the hole in $HO − iH + 1$). For $iE = 3$, the time evolution of the populations of Kohn-Shan orbitals LU, $LU + 1$, and $LU + 2$ is determined by the part of equations of motion involving perturbed orbitals as following:

$$\frac{d\rho_{LU,LU}}{dt} = R_{LU,LU+1}\rho_{LU+1,LU+1} + R_{LU,LU+2}\rho_{LU+2,LU+2} \tag{13a}$$

$$\frac{d\rho_{LU+1,LU+1}}{dt} = -R_{LU,LU+1}\rho_{LU+1,LU+1} + R_{LU+1,LU+2}\rho_{LU+2,LU+2} \tag{13b}$$

$$\frac{d\rho_{LU+2,LU+2}}{dt} = -R_{LU+1,LU+2}\rho_{LU+2,LU+2} − R_{LU,LU+2}\rho_{LU+2,LU+2} \tag{13c}$$

The initial conditions are $\rho_{11}(t = 0) = 0$, $\rho_{22}(t = 0) = 0$, and $\rho_{33}(t = 0) = 1$. The solutions are shown in Supporting Information (eqs S1a−S1c). A diagram illustrating partitioning of Liouville space, used in eq 13 is shown in Figure 5. The analytical results reproduce very well time evolutions of the KS orbital populations obtained from numerical solutions. Figure 6 illustrates the analytic and numerical results of time evolutions of the occupations of KS orbitals for the excited state $iE = 3$ and the numerical result for $iE = 8$ of the bare NW. For $iE = 3$, the population in $LU + 2$ is 1 at $t = 0$, and it decays rapidly with time. There are small differences between numerical and analytical results when approaching $t = 1$ ps for $LU + 2$. The population in $LU + 1$ is increased from 0 to 0.9 in less than 1 ps, and then decreased gradually. The population in LU is increased gradually with the time. When $t < 0.01$ ps, the numerical solution has a stepwise raising character, deviating slightly from the analytical solution. Similarly, for $iE = 8$, the population in $LU + 7$ is 1 at $t = 0$, and it decays rapidly with the time. The population in LU is increased from 0 to 1 gradually
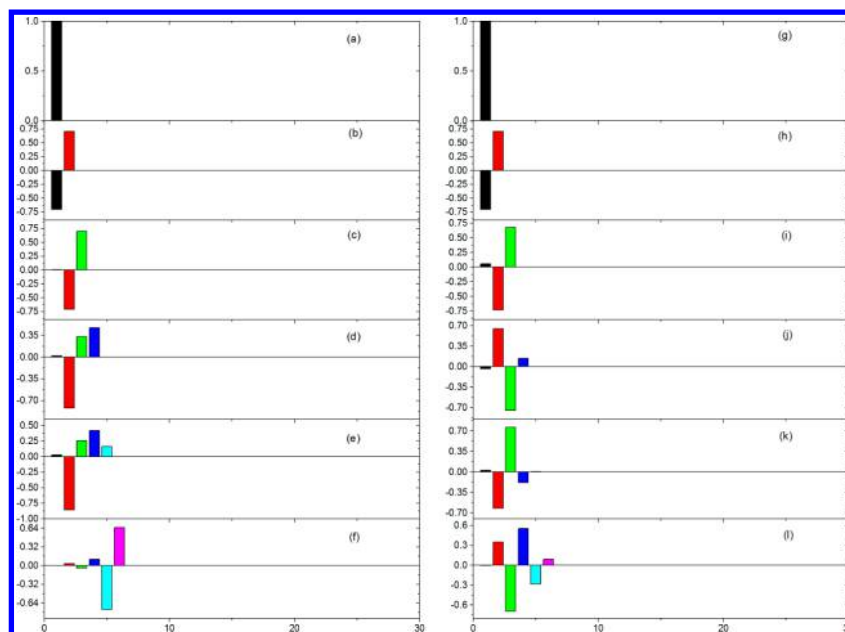
Figure 4. Eigenvectors of intraband Liouville−Redfield superoperators for electrons and holes. (a)−(f) First ∼ sixth eigenvectors for electron. (g)−(l) The first ∼ sixth eigenvectors for hole. The horizontal ordinate labels the index of an orbital. The longitudinal coordinates represent eigenvectors of the Liouville−Redfield superoperator in basis of KS orbitals. The values of ρ_{ij}^{v} for $i = j$ are illustrated from eq 6a−6c. Therefore, the horizontal ordinate has only one index $i = j$.
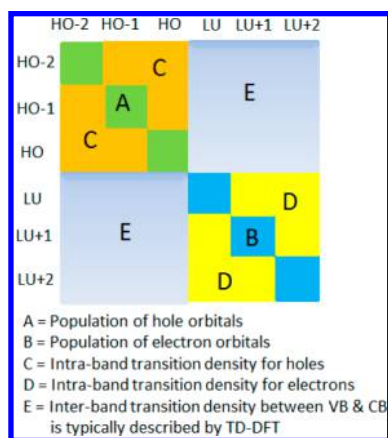

Figure 5. Partitioning of Liouville space illustrating eq 13.

with the time. During the relaxation, the peak value of the population follows the trend: $P_{LU+1}^{max} > P_{LU+4}^{max} > P_{LU+6}^{max} > P_{LU+3}^{max} > P_{LU+2}^{max}$.

Table 1 displays the nonadiabatic relaxation rates obtained from analytical and numerical solutions for the bare TiO$_2$ NW and bulk TiO$_2$. For the excited state $iE = 2$ (the electron is initially at $LU + 1$), K_e is assumed to be equal to $R_{LU,LU+1}$ (the population transfer rate from $LU + 1$ to LU) by only considering the electron transitions from high energy levels to low ones. For the bare NW, $R_{LU,LU+1} = 0.1741$ ps^{-1}. The K_e ($iE = 2$) obtained from the single exponential fit is 0.1907 ps^{-1}, close to the analytic solution. Similarly the analytic solution for $iH = 2$ is $K_h(iH = 2) = R_{HO,HO-1}$. The single exponential fit of the energy relaxation rate is well suited for the initial conditions $iE = 2$ and $iH = 2$ of the bare NW. For the excited state $iE = 3$, the electron relaxation rates are composed of three elements: $R_{LU,LU+2}$, $R_{LU+1,LU+2}$, and $R_{LU,LU+1}$. And there are two relaxation channels: $LU + 2 \rightarrow LU$ and $LU + 2 \rightarrow LU + 1 \rightarrow LU$. We add together the rates for the two channels

$$K_e(iE = 3) = R_{LU,LU+2} + \frac{R_{LU+1,LU+2}R_{LU,LU+1}}{R_{LU+1,LU+2} + R_{LU,LU+1}}$$

The K_e ($iE = 3$) obtained from the numerical solution is larger than the analytic solution for both the bare NW and bulk. The analytical solution for $iH = 3$ is similar to the one for $iE = 3$. For $iE = 4$, there are four relaxation channels

$$LU + 3 \rightarrow LU$$

$$LU + 3 \rightarrow LU + 2 \rightarrow LU$$

$$LU + 3 \rightarrow LU + 1 \rightarrow LU$$

$$LU + 3 \rightarrow LU + 2 \rightarrow LU + 1 \rightarrow LU$$

The K_e ($iE = 4$) or K_h ($iH = 4$) obtained from the numerical solution for the bare NW is smaller than the analytic solution. For TiO$_2$ bulk, the K_e ($iE = 2, 3$) obtained from the numerical solution is much larger than its analytic solution. This can be explained by the fact that in the TiO$_2$ bulk the energies of orbitals are spaced densely, whereas in NW, energies of orbitals are spaced sparsely. Larger $\Delta\varepsilon$ subgap between nearest orbitals delays the dissipation. As it miss matches resonance between electronic transition energy and phonon normal-mode frequency. This observation supports phonon bottleneck hypothesis.[77,78]

Figure 7 shows the nonadiabatic relaxation dynamics for initial conditions corresponding to two bright optical transitions and partial charge densities for orbitals corresponding to transitions ($HO, LU + 7$) and ($HO − 23, LU + 2$) at Γ point representing initial states during the dynamics. The nonadiabatic relaxation dynamics of the strongest optical transition (with the largest oscillator strength) and the partial charge densities for its corresponding transition orbitals are shown in Supporting Information Figure S1. Here, we provide analysis of dynamics for electron and hole parts of an excitation. In the simplest case, the nonradiative relaxations of electron starting in LU and hole starting in HO at $t = 0$ show trivial
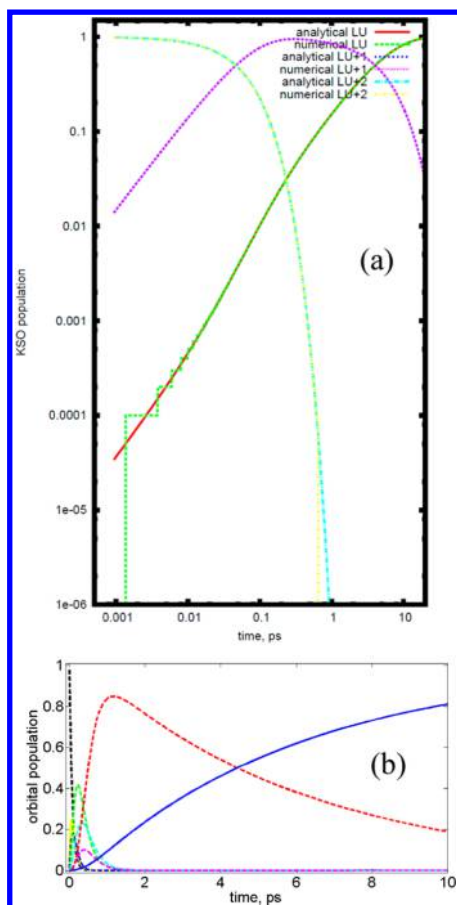
Figure 6. (a) Numerical and analytical results of occupations of KS orbitals with time for $iE = 3$ of the bare NW. The y axis is intentionally expanded for highlighting the vanishing difference of analytical and numerical results. (b) Numerical result of occupations of KS orbitals with time for $iE = 8$ of the bare NW. The blue solid, red dash, magenta dash, cyan dash, green dash, blue dash, yellow solid, and black dash lines stand for population changes of LU, $LU + 1$, $LU + 2$, $LU + 3$, $LU + 4$, $LU + 5$, $LU + 6$, and $LU + 7$.

Table 1. Non-Adiabatic Relaxation Rates of the Bare TiO$_2$ NW and TiO$_2$ Bulk from Analytical and Numerical Solutions, in Which Units the Are ps^{-1A}

	bare TiO$_2$ NW		TiO$_2$ bulk	
	analytical data	numerical data	analytical data	numerical data
$iE = 2$	0.1741	0.1907	0.0235	0.0975
$iE = 3$	0.2075	0.2939	0.0322	0.2066
$iE = 4$	0.3197	0.2950	0.3951	0.3922
$iH = 2$	0.8784	0.8884	13.6152	13.7709
$iH = 3$	1.1592	1.8092	10.0206	11.5972
$iH = 4$	2.4184	1.5942	11.2137	10.4945

^{A}In bulk, holes relax 5−10 times faster than in the NW. It shows that quantum confinement in NW slows down the relaxation in agreement with theoretically predicted "phonon bottleneck" effect, that is, orbitals in VB of NW become sparse and do not match resonance condition with normal modes frequencies.

behavior: distributions $n(\varepsilon,t)$ are flat as there is nowhere to go. This corresponds to the solution $\rho_{LU,LU}(t) = 1 = const$ and $\rho_{HO,HO}(t) = 1 = const$. The nonradiative relaxation of hole starting in $HO − 27$ at $t = 0$ is close to the one of hole starting in $HO − 28$ (See Table 2). The partial charge density analysis showing that the electron relaxation to LU involves a
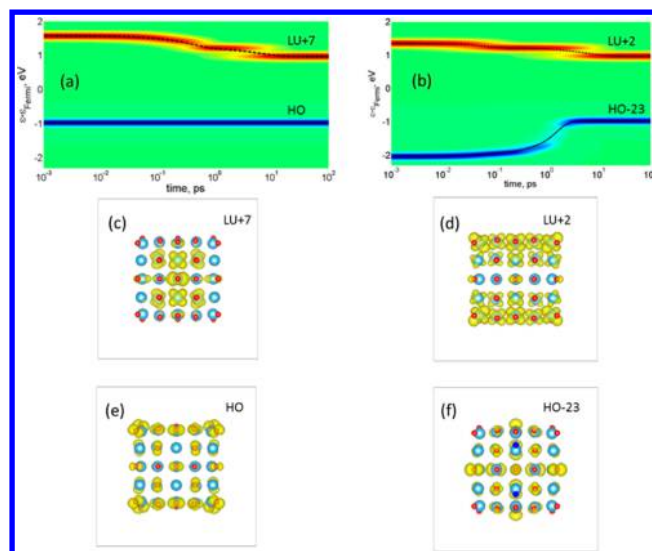

Figure 7. (a)−(b) Nonadiabatic relaxation dynamics of the two optical transitions of $\langle 001 \rangle$ NW. Here, red, green, and blue colored areas label the distribution $\Delta n^{(a,b)}(\varepsilon, t)$ in eq 7 for gain, no change, and loss, respectively, in comparison with the equilibrium distribution; red areas can be understood as relating to electrons, and blue ones to holes. (c)−(f) The top views of partial charge densities for $(HO, LU + 7)$ and $(HO − 23, LU + 2)$ pairs of orbitals at Γ point. Ti atoms are in blue, and O atoms are in red. Partial charge density for HO concentrates on edge/step under-coordinated ions. LU orbital is delocalized. Thus, transition $HO \rightarrow LU$ has charge transfer character and vanishing oscillator strength.

Table 2. Electron and Hole Energy Dissipation Rates K_e and K_h of Featured Electronic Transitions of the Studied Bare NW^a

transition energy (eV)	oscillator strength	hole index (iH)	electron index (iE)	K_e, ps^{-1}	K_h, ps^{-1}	$K_e + K_h$, ps^{-1}
2.9232	0.4369	1	8	0.4009	0.0	0.4009
2.9241	0.4342	2	9	0.4154	0.8884	1.3038
3.1179	1.3215	28	1	0.0	0.7340	0.7340
3.1197	1.3187	29	1	0.0	0.7264	0.7264
3.2395	0.4770	4	21	0.5117	1.5942	2.1059
3.4181	0.5750	24	3	0.2939	0.8077	1.1016
3.4196	0.5753	24	4	0.2950	0.8077	1.1027
3.4712	0.4482	21	5	0.3312	0.8420	1.1732
3.4763	0.4566	22	5	0.3312	0.7754	1.1066

^{a}Note that most probable transition promotes an electron from deep in the VB ($iH = 28, 29$) to the bottom of CB ($iE = 1$).

subsequent transition between several Ti 3d orbitals while the holes relaxing to HO subsequently occupy several surface O 2p orbitals. The hole arrives to the surface earlier than electron. During the time interval between $(K_h^{-1}) < t < (K_e^{-1})$, the surface of NW is positively charged. Consequently, the hole can facilitate oxidation of water.

The probable photoexcitations and their relaxation nonequilibrium dynamics of the bare NW are summarized in Table 2. The energies of bright transitions are higher than the optical band gap energies. Most probable transitions with high oscillator strength ($\sim$1.32) occur from deep in the valence band to the edge of conduction band. The two relaxation rates for the most probable transitions are most likely to be observed in experiment.
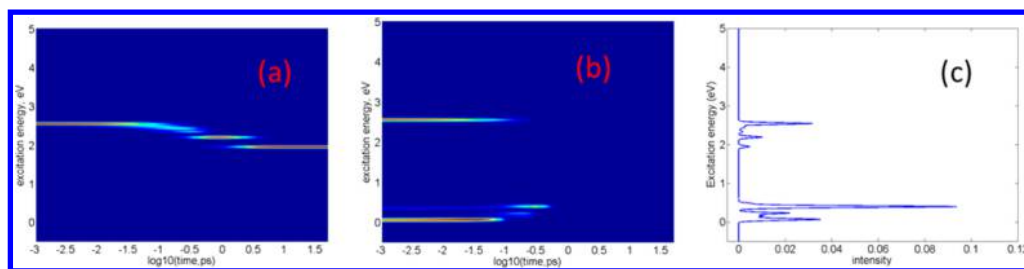
Figure 8. (a) Simulated photoexcitation dynamics, (b) emission dynamics, and (c) integrated emission spectra of bare TiO_2 NW after photoexcitation corresponding to the transition from HO to $LU + 7$. Colors correspond to the intensity (oscillator strength) of transition scaled accordingly to the rainbow order: red stays for maximum intensity and navy blue for zero. Interestingly, low emission at band gap energy may indirectly witness formation of charge transfer state.

Electron and hole relaxations have different dependence on energy. The hole created deep in the valence band takes longer to relax to the HO. The hole relaxes faster in energy than the electron due to different spacing of orbital energies in valence bands (VBs) and conduction bands (CB). The hole relaxation rates of the bare NW are smaller than those of bulk TiO_2 (Supporting Information Table S2) and (101) surface (Supporting Information Table S3) due to sparse spacing of orbitals' energies originating from quantum confinement, in agreement with phonon bottleneck hypothesis. We analyze the relaxation of the most probable optical transition of the bare NW, which occurs between an occupied KS orbital deep in the valence band and unoccupied KS orbital at the edge of conduction band. For this excitation, the excited hole experiences nonradiative relaxation in energy from an orbital located deep in the valence band to the HO within 1.4 ps. There are no experimental or computational studies on the nonadiabatic excited dynamics of the bare TiO_2 NW. But there was a real-time TDDFT study of natural-dye sensitized TiO_2 NW solar cells using cyanidin as a model molecule, which showed that excited electrons are injected from the natural-dye to the conduction band of TiO_2 at the ultrafast time scale of 50 fs.[28] The nonadiabatic coupling calculations on the surface functionalized TiO_2 NW are underway. We will compare the carrier relaxation rates of the bare NW with the surface functionalized TiO_2 NW. The experimental studies of the hot carrier relaxation in TiO_2 NW are possible by femtosecond spectroscopy techniques.[79]

The simulated photoexcitation dynamics, emission dynamics, and integrated emission spectrum of the TiO_2 NW after photoexcitation corresponding to HO → LU+7 transition are shown in Figures 8a−c. Figure 8a shows that the excitation, corresponding to the parent interband absorption from HO to $LU + 7$, has a nonradiative lifetime of 0.1 ps at $LU + 7$ orbital. The electron stays at an orbital between $LU + 7$ and LU at 0.3− 3 ps, and stays at the edge of the band gap after 3 ps. The emission dynamics in Figure 8b shows an emission signal at ~2.6 eV disappears within 0.1 ps. Figure 8c shows the signal below 2.6 eV, which is due to band edge luminescence. This is in agreement with the emission dynamics results. There are additional intraband emission features at IR-range energies less than 1.0 eV, corresponding to the radiative intraband transitions from CB to CB or VB to VB for the photoexcited electron or hole. These radiatively allowed transitions with the energies smaller than the band gap can be observed in ultrafast time-resolved pump−probe spectroscopies. Low intensity of emission at bandgap energy may witness formation of charge transfer from surface to inner layers of NW.

4. CONCLUSIONS

In summary, we have investigated the electronic structure and electronic dissipative dynamics originating from electron− lattice vibration nonadiabatic couplings of ⟨001⟩ anatase TiO_2 NW by combining density matrix formalism and ab initio electronic structure calculations. The properties of eigenvectors of Liouville superoperators are investigated. Eigenvectors ρ_v are analyzed by decomposition in basis of k Kohn−Sham orbitals contributing to ρ_v. For example, the first element of the first eigenvector of electron or hole is the contribution of the orbital LU or HO to the first eigenvector. The first and second eigenvectors of electron and hole are the same. The sum of the square of each element of a given eigenvector is 1. Nonzero elements of eigenvector exhibit sign alternation. A super-position of those eigenvectors weighted by time evolution factors that include eigenvalues of Liouville superoperator represents dissipative dynamics of density matrix for given initial conditions. The analytical and numerical results on the electron and hole relaxation rates are compared. The time evolutions of orbital populations obtained by analytical solutions are in agreement with the numerical results obtained via diagonalization of Liouville superoperator. The electron nonradiative relaxation to the bottom of the conduction band involves population of Ti 3d orbitals, whereas the hole nonradiative relaxation to the top of the valence band involves O 2p orbitals. Comparison of the dissipation rates for NW and bulk TiO_2 indicates signatures of phonon bottleneck effect for hole relaxation, that is, in NW, relaxation of holes is slowed down by 5−10 times. This result was not possible to predict without computation because the hypothesis of phonon-bottleneck is very sensitive to specific surface reconstruction/ functionalization. For example it fails for CdSe and PbSe nanocrystals in both experiment and theory.[80] Interestingly, computed emission spectra has low intensity at bandgap energy. Such observation may witness charge transfer state formation. Obtained insights into photoinduced dynamics help in design of efficient materials for photoelectrochemical water splitting.

■ ASSOCIATED CONTENT

Ⓢ Supporting Information
Eigenfrequencies, electron and hole energy dissipation rates, and analytic solutions. This material is available free of charge via the Internet at http://pubs.acs.org.

■ AUTHOR INFORMATION

Corresponding Author
*E-mail: Dmitri.Kilin@usd.edu.

■ **REFERENCES**

(1) Nowotny, J. *Oxide Semiconductors for Solar Energy Conversion: Titanium Dioxide*. CRC Press, Taylor &Francis Group: Boca Raton, 2012.

(2) Fujishima, A.; Honda, K. *Nature* **1972**, *238*, 37−38.

(3) Pelizzetti, E.; Minero, C.; Borgarello, E.; Tinucci, L.; Serpone, N. *Langmuir* **1993**, *9*, 2995−3001.

(4) Katoh, R.; Furube, A.; Yamanaka, K.-i.; Morikawa, T. *J. Phys. Chem. Lett.* **2010**, *1*, 3261−3265.

(5) Chen, X.; Mao, S. S. *Chem. Rev.* **2007**, *107*, 2891−2959.

(6) Cozzoli, P. D.; Comparelli, R.; Fanizza, E.; Curri, M. L.; Agostiano, A.; Laub, D. *J. Am. Chem. Soc.* **2004**, *126*, 3868−3879.

(7) Diebold, U. *Surf. Sci. Rep.* **2003**, *48*, 53−229.

(8) Li, G.; Li, L.; Boerio-Goates, J.; Woodfield, B. F. *J. Am. Chem. Soc.* **2005**, *127*, 8659−8666.

(9) Barnard, A. S.; Curtiss, L. A. *Nano Lett.* **2005**, *5*, 1261−1266.

(10) Nakade, S.; Saito, Y.; Kubo, W.; Kitamura, T.; Wada, Y.; Yanagida, S. *J. Phys. Chem. B* **2003**, *107*, 8607−8611.

(11) Moon, W.-T.; Lee, K.-S.; Jun, Y.-K.; Kim, H.-S.; Hong, S.-H. *Sens. Actuators, B* **2006**, *115*, 123−127.

(12) Huang, S.-P.; Xu, H.; Bello, I.; Zhang, R.-Q. *Chem.—Eur. J.* **2010**, *16*, 13072−13076.

(13) Asahi, R.; Morikawa, T.; Ohwaki, T.; Aoki, K.; Taga, Y. *Science* **2001**, *293*, 269−271.

(14) Chrétien, S.; Metiu, H. *Catal. Lett.* **2006**, *107*, 143−147.

(15) Kim, H. Y.; Lee, H. M.; Pala, R. G. S.; Shapovalov, V.; Metiu, H. *J. Phys. Chem. C* **2008**, *112*, 12398−12408.

(16) Ito, T.; Wang, J. X.; Lin, C. H.; Lunsford, J. H. *J. Am. Chem. Soc.* **1985**, *107*, 5062−5068.

(17) Jensen, S.; Kilin, D. *Int. J. Quantum Chem.* **2012**, *112*, 3874−3878.

(18) Zhang, Y.; Kilin, D. S. *Int. J. Quantum Chem.* **2012**, *112*, 3867−3873.

(19) Inerbaev, T. M.; Hoefelmeyer, J. D.; Kilin, D. S. *J. Phys. Chem. C* **2013**, *117*, 9673−9692.

(20) Grunes, L. A.; Leapman, R. D.; Wilker, C. N.; Hoffmann, R.; Kunz, A. B. *Phys. Rev. B* **1982**, *25*, 7157−7173.

(21) Rino, J.-P.; Studart, N. *Phys. Rev. B* **1999**, *59*, 6643−6649.

(22) Sousa, C.; Illas, F. *Phys. Rev. B* **1994**, *50*, 13974−13980.

(23) Fahmi, A.; Minot, C.; Silvi, B.; Causá, M. *Phys. Rev. B* **1993**, *47*, 11717−11724.

(24) Gong, X.-Q.; Selloni, A.; Batzill, M.; Diebold, U. *Nat. Mater.* **2006**, *5*, 665−670.

(25) Lee, J. H.; Hevia, D. F.; Selloni, A. *Phys. Rev. Lett.* **2013**, *110*, 016101.

(26) Tafen, D. N.; Lewis, J. P. *Phys. Rev. B* **2009**, *80*, 014104.

(27) Deák, P.; Aradi, B.; Gagliardi, A.; Huy, H. A.; Penazzi, G.; Yan, B.; Wehling, T.; Frauenheim, T. *Nano Lett.* **2013**, *13*, 1073−1079.

(28) Meng, S.; Ren, J.; Kaxiras, E. *Nano Lett.* **2008**, *8*, 3266−3272.

(29) Tully, J. C. *J. Chem. Phys.* **1990**, *93*, 1061−1071.

(30) Pechukas, P. *Phys. Rev.* **1969**, *181*, 174−185.

(31) Nelson, T.; Fernandez-Alberti, S.; Roitberg, A. E.; Tretiak, S. *J. Chem. Phys.* **2013**, *138*, 224111.

(32) Fang, J.-Y.; Hammes-Schiffer, S. *J. Chem. Phys.* **1999**, *110*, 11166−11175.

(33) Sholl, D. S.; Tully, J. C. *J. Chem. Phys.* **1998**, *109*, 7702−7710.

(34) Tully, J. C. *Classical and Quantum Dynamics in Condensed Phase Simulations*; World Scientific Publishing Company: Singapore, 1998.

(35) Meyera, H. D.; Miller, W. H. *J. Chem. Phys.* **1979**, *70*, 3214−3223.

(36) Stock, G.; Thoss, M. *Phys. Rev. Lett.* **1997**, *78*, 578−581.

(37) Redfield, A. G. *IBM J. Res. Dev.* **1957**, *1*, 19−31.

(38) Egorova, D.; Thoss, M.; Domcke, W.; Wang, H. B. *J. Chem. Phys.* **2003**, *119*, 2761−2773.

(39) Pollard, W. T.; Friesner, R. A. *J. Chem. Phys.* **1994**, *100*, 5054−5065.

(40) Pollard, W. T.; Felts, A. K.; Friesner, R. A. The Redfield equation in condensed-phase quantum dynamics. In *Advances in Chemical Physics*; Wiley-VCH: Weinheim, Germany, 1996; Vol 93, pp 77−134.

(41) Jean, J. M.; Friesner, R. A.; Fleming, G. R. *J. Chem. Phys.* **1992**, *96*, 5827−5842.

(42) Leggett, A. J.; Chakravarty, S.; Dorsey, A. T.; Fisher, M. P. A.; Garg, A.; Zwerger, W. *Rev. Mod. Phys.* **1987**, *59*, 1−85.

(43) Duncan, W. R.; Stier, W. M.; Prezhdo, O. V. *J. Am. Chem. Soc.* **2005**, *127*, 7941−7951.

(44) Duncan, W. R.; Prezhdo, O. V. *J. Am. Chem. Soc.* **2008**, *130*, 9756−9762.

(45) Prezhdo, O. V.; Duncan, W. R.; Prezhdo, V. V. *Acc. Chem. Res.* **2008**, *41*, 339−348.

(46) Duncan, W. R.; Prezhdo, O. V. *Annu. Rev. Phys. Chem.* **2007**, *58*, 143−184.

(47) Akimov, A. V.; Neukirch, A. J.; Prezhdo, O. V. *Chem. Rev.* **2013**, *113*, 4496−4565.

(48) Craig, C. F.; Duncan, W. R.; Prezhdo, O. V. *Phys. Rev. Lett.* **2005**, *95*, 163001.

(49) Fischer, S. A.; Habenicht, B. F.; Madrid, A. B.; Duncan, W. R.; Prezhdo, O. V. *J. Chem. Phys.* **2011**, *134*, 024102.

(50) Habenicht, B. F.; Prezhdo, O. V. *Phys. Rev. Lett.* **2008**, *100*, 197402.

(51) Fischer, S. A.; Duncan, W. R.; Prezhdo, O. V. *J. Am. Chem. Soc.* **2009**, *131*, 15483−15491.

(52) Long, R.; English, N. J.; Prezhdo, O. V. *J. Am. Chem. Soc.* **2012**, *134*, 14238−14248.

(53) Long, R.; Prezhdo, O. V. *J. Am. Chem. Soc.* **2011**, *133*, 19240−19249.

(54) Rego, L. G. C.; Batista, V. S. *J. Am. Chem. Soc.* **2003**, *125*, 7989−7997.

(55) Schatz, G. C.; Ratner, M. A. Quantum Mechanics in Chemistry. In *Quantum Mechanics in Chemistry*; Prentice-Hall: Englewood Cliffs, NJ, 1993.

(56) Huang, S.; Kilin, D. S. *Mol. Phys.* **2013**, *112*, 539−545.

(57) Huang, S.; Kilin, D. S. *MRS Proceedings* **2013**, *1659*, No. 10.1557/opl.2014.354.

(58) Huang, S.; Inerbaev, T. M.; Kilin, D. S. *J. Phys. Chem. Lett.* **2014**, *5*, 2823−2829.

(59) Kohn, W.; Sham, L. J. *Phys. Rev.* **1965**, *140* (4A), 1133−1138.

(60) Perdew, J. P.; Zunger, A. *Phys. Rev. B* **1981**, *23*, 5048−5079.

(61) Perdew, J. P.; Chevary, J. A.; Vosko, S. H.; Jackson, K. A.; Pederson, M. R.; Singh, D. J.; Fiolhais, C. *Phys. Rev. B* **1992**, *46*, 6671−6687.

(62) Perdew, J. P.; Burke, K.; Ernzerhof, M. *Phys. Rev. Lett.* **1996**, *77*, 3865−3868.

(63) Henderson, T. M.; Izmaylov, A. F.; Scalmani, G.; Scuseria, G. E. *J. Chem. Phys.* **2009**, *131*, 044108.

(64) Kresse, G.; Furthmuller, J. *Phys. Rev. B* **1996**, *54*, 11169−11186.

(65) Blöchl, P. E. Projector augmented-wave method. *Phys. Rev. B* **1994**, *50*, 17953−17979.

(66) Vazhappilly, T.; Kilin, D. S.; Micha, D. A. J. *Phys. Chem. C* **2012**, *116*, 25525−25536.

(67) Kryjevski, A.; Kilin, D.; Kilina, S. J. *Renewable Sustainable Energy* **2013**, *5*, 043120.

(68) Mukamel, S. *Principles of nonlinear optical spectroscopy*; University Press: Oxford, 1995.

(69) Kilin, D. S.; Micha, D. A. *J. Phys. Chem. Lett.* **2010**, *1*, 1073−1077.

(70) May, V., Kuhn, O. *Charge and Energy Transfer Dynamics in Molecular Systems*; Wiley-VCH: Berlin, Germany, 2000.

(71) Kilin, D. S.; Micha, D. A. *J. Phys. Chem. C* **2010**, *115*, 770−775.

(72) Hammes-Schiffer, S.; Tully, J. C. *J. Chem. Phys.* **1994**, *101*, 4657−4667.

(73) Fischer, S. A.; Habenicht, B. F.; Madrid, A. B.; Duncan, W. R.; Prezhdo, O. V. *J. Chem. Phys.* **2011**, *134*, 024102.

(74) Gebauer, R.; Burke, K.; Car, R. Kohn-Sham Master Equation Approach to Transport Through Single Molecules. In *Time-Dependent Density Functional Theory*; Marques, M. L., Ullrich, C., Nogueira, F., Rubio, A., Burke, K., Gross, E. U., Eds. Springer: Berlin Heidelberg, 2006; Vol. *706*, pp 463−477.

(75) Usuda, M.; Hamada, N.; Kotani, T.; van Schilfgaarde, M. *Phys. Rev. B* **2002**, *66*, 125101.

(76) Godby, R. W.; Schlüter, M.; Sham, L. J. *Phys. Rev. Lett.* **1986**, *56*, 2415−2418.

(77) (a) Yoffe, A. D. *Adv. Phys.* **2001**, *50*, 1−208. (b) Klimov, V. I.; McBranch, D. W.; Leatherdale, C. A.; Bawendi, M. G. *Phys. Rev. B* **1999**, *60*, 13740−13749.

(78) Nozik, A. J. *Annu. Rev. Phys. Chem.* **2001**, *52*, 193−231.

(79) Pensack, R. D.; Banyas, K. M.; Asbury, J. B. *J. Phys. Chem. C* **2009**, *114*, 5344−5350.

(80) Kilina, S.; Kilin, D. S.; Prezhdo, O. V. *ACS Nano* **2009**, *3*, 93−99.